Materials & Design 217 (2022) 110632

Contents lists available at ScienceDirect

Materials & Design

journal homepage: www.elsevier.com/locate/matdes

Microwave driven synthesis of narrow bandgap alpha-tin nanoparticles on silicon

I. Mazzetta [a,*], L. Viti [b], F. Rigoni [c], S. Quaranta [d], A. Gasparotto [e], G. Barucca [f], F. Palma [a], P. Riello [c], E. Cattaruzza [c], M. Asgari [b], M. Vitiello [b], F. Irrera [a]

[a] Department of Information Technology, Electronics and Telecommunications, Sapienza University of Rome, Rome, Italy
[b] NEST, CNR - Istituto Nanoscienze and Scuola Normale Superiore, Pisa, Italy
[c] Department of Molecular Sciences and Nanosystems, Ca' Foscari University of Venice, Mestre, Italy
[d] Institute for the Study of Nanostructured Materials (ISMN) – Italian National Research Council, Rome, Italy
[e] Department of Physics and Astronomy "G. Galilei", University of Padova, Padova, Italy
[f] Department of Materials, Environmental Sciences and Urban Planning, Marche Polytechnic University, Ancona, Italy

HIGHLIGHTS

- A CMOS-compatible MW-driven process resulting into α-Sn over Si was proposed.
- A 52 meV direct bandgap was extrapolated from FTIR measurements.
- An α-Sn phase stable up to 200 °C was synthesized.
- MW-enhanced atomic diffusion and fast cooling may favor formation of α-Sn domains.
- α-Sn domains/amorphous oxide core/shell structure was found.

GRAPHICAL ABSTRACT

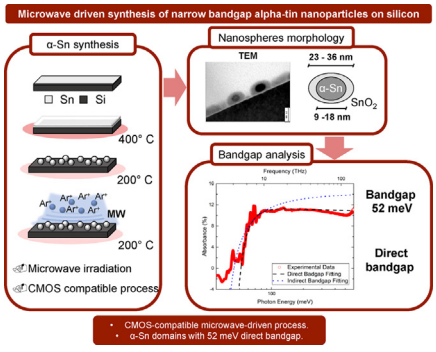

ARTICLE INFO

Article history:
Received 7 December 2021
Revised 4 April 2022
Accepted 5 April 2022
Available online 8 April 2022

ABSTRACT

This work proposes a microwave-based synthetic route for the preparation of tin nanospheres with a diamond-like α-phase structure on silicon. The main characteristics of the synthesized material are an extraordinarily narrow (around 50 meV) direct bandgap and an improved thermal stability (up to 200° C). Structural and compositional characterizations showed a core–shell structure comprised of an outer amorphous oxide shell and inner core containing α-phase tin domains. Microwaves turned out to be instrumental in achieving the specific nanostructures reported, due to their peculiar heating characteristics. Low pressure, low temperature and compatibility with integrated circuits manufacturing represent the most innovative features of the present synthetic process.

1. Introduction

Silicon is the most widespread semiconductor for consumable electronics. However, silicon use in photonics has been hindered by intrinsic physical issues practically impeding its application as both light emitter and detector in certain wavelength ranges. First of all, silicon indirect bandgap precludes direct transitions from the lower edge of the conduction band to the valence band, hampering efficient emission of light. In addition, its relative wide bandgap energy (E_g = 1.12 eV at room temperature) prevents silicon from absorbing light in the medium and far infrared (MIR and FIR, respectively) regions.

* Corresponding author.
E-mail address: ivan.mazzetta@uniroma1.it (I. Mazzetta).

https://doi.org/10.1016/j.matdes.2022.110632
0264-1275/

Small bandgap semiconductors, suitable for integration on silicon, are expected to combine light absorption in the MIR range and large-scale manufacturing. For instance, integration of germanium on silicon may extend the range of usable wavelengths. Indeed, both Ge direct (0.8 eV) and indirect (0.64 eV) transitions can be tuned by introducing a tensile strain caused by lattice mismatch between the two semiconductors [1–3]. On the other hand, different approaches relying on heavy doping of Ge nanostructures on Si substrates have proved to be successful. For example, a 0.77 eV bandgap was attained by doping Ge with phosphorous, while E_g dropped to 0.5 eV when chemical deposition of a Si_3N_4 film on top of doped germanium nanopillars was performed [4]. High-quality epitaxially-grown layers and quantum-engineered heterostructures have also paved the way for group IV materials integration in infrared photonics. Therefore, (Si)GeSn semiconductors have emerged as new materials for photonic applications [5]. Nevertheless, the ability to tune lattice and electronic parameters is crucial to fabricate a large variety of heterostructures and low-dimensional systems based on group IV materials. Group IV alloys are versatile building blocks for silicon compatible infrared detectors, sensors, and emitters, for applications in free-space communication, infrared energy harvesting, biological and chemical sensing, and thermal imaging [6,7].

Among IV-group elements, tin is particularly intriguing because of low extraction costs, natural abundance and excellent compatibility with silicon. β-Sn and α-Sn, or gray tin, are the only two thermodynamically stable Sn phases. β-Sn has a body centered tetragonal structure, whose lattice parameters are a = b = 5.8318 Å and c = 3.1819 Å, and shows a metallic behavior. Conversely, α-Sn has a face-centered diamond cubic crystal structure with lattice constant of 6.4892 Å and it is characterized by a very peculiar band structure. α-Sn can be categorized as a zero-gap semiconductor with a direct bandgap of −0.41 eV [8–10]. The conduction and valence bands overlap only for certain wavevectors (k) resulting in a semi-metallic behavior. Thus, α-Sn can be considered a semiconductor for most of k. These characteristics make α-Sn particularly appealing for silicon-based photonics, but its usage has been hampered, up to date, by α-Sn instability at room temperature: α-Sn transition to β-Sn takes place spontaneously at 13.2 °C. However, α-Sn properties can be manipulated on a nanoscale level to extend its metastability temperature range. For instance, α-Sn nanocrystals obtained by micro-plasma synthesis in ethanol suspensions proved to be stable at room temperature. Furthermore, crystal size and quantum confinement were found to impact significantly on the bandgap extension [11]. Also, the inclusion of heteroatoms in the α-Sn lattice can raise the transition temperature and shift the Fermi level [12,13]. Oehl et al. reported a stability range up to 90 °C for bulk α-Sn alloyed with 0.6 wt% silicon prepared by melt spinning [14]. Conversely, α-Sn films epitaxially grown on InSb were demonstrated to be stable up to 200 °C [15]. Lattice mismatches with respect to silicon substrate are 19.5% and 7.4%, for α-Sn and β-Sn, respectively. Consequently, the metallic β-phase formation is generally favored when epitaxial growth is performed. Nonetheless, 3.5 monolayers of α-Sn were found to grow underneath β-Sn on (1 1 1) silicon [16,17]. The progressive transition of α-Sn to β-Sn with increasing thickness was explained by the low free energy of bulk β-phase compared to epitaxial α-Sn. It is worth noticing that lattice mismatch can bring about either a bandgap widening or reduction according to the specific strain generated [18]. Narrow direct bandgap α-Sn thin films were grown by Molecular Beam Epitaxy on CdTe and InSb substrates [9,19]. Bandgap energy values of hundreds of meV were attained for particle sizes of a few nanometers, and a progressive bandgap narrowing was predicted for higher diameters [11,20]. Finally, the growth of amorphous α-Sn layers was also accomplished on amorphous silicon substrates [21]. Thus, it can be inferred that three main reasons seem to promote the stabilization and bandgap widening (or narrowing) of α-Sn: dopant atoms inclusion, mechanical strain, and nanostructured size.

In light of pursuing new techniques for growing narrow bandgap materials, the present paper proposes the preparation of α-Sn-based nanostructures compatible with microelectronics manufacturing. The α-Sn synthetic route requires exposing silicon wafers randomly covered by Sn nanospheres (NS) to microwaves (MWs) in a chemical vapor deposition (CVD) reactor (MW-CVD reactor). Possible reasons underlying the formation of α-Sn phase reside in the irradiation of the sample by microwaves, in lattice mismatch stemming from Sn doping by silicon, and in the nanometric size of tin particles. In particular, microwave heating offers plenty of advantages over conventional heating, such as: radiative energy transfer, instead of heat propagation by thermal conduction and convection; rapid, material selective and volumetric heating; fast power switching. Finally, the proposed method is amenable to large-scale production because of the low pressure and temperatures involved in the process.

Optical absorption measurements performed on a large set of samples, revealed an absorption edge around 50 meV and a direct bandgap only for the MW irradiated samples. Accordingly, microwave exposure is instrumental in the formation of the α-Sn and direct bandgap widening. The synthesized α-Sn is thermodynamically stable from room temperature to at least 200 °C.

The paper is organized as follows: Section 2 describes the process leading to the nanospheres containing the tin α-phase and the characterization techniques used to investigate their compositional, structural and optical properties; Section 3 reports the characterization results; Section 4 discusses the work achievements and proposes a phenomenological picture of the mechanism underlying the formation of α-Sn domains and the role of microwaves; Section 5 concludes the paper.

2. Material and characterization

2.1. Treatment in the MW-CVD reactor

A set of (1 0 0) silicon wafers, both intrinsic and doped (either p-type and n-type), with a 70 nm SiOx film deposited by Plasma Enhanced Chemical Deposition (PECVD) on top were used as substrates. Wafers were cleaned according to the method devised by Radio Corporation of America (RCA) to remove ionic and organic contaminants. The steps leading to the formation of the nanostructured material on silicon substrate are summarized in Fig. 1. Briefly, a quasi-uniform 5 nm-thick Sn film was thermally evaporated on the wafer surface (step a). Then, the samples were introduced in a CVD reactor and heated up to ∼ 400° C (baking step) with a fixed rate of 1° C/s, in order to melt the metal (step b). Subsequently, samples were left cooling down until the surface reached a temperature of ∼ 200 °C (cooling step). In this step, the metal clustered in particles of nanometric size (step c). Baking and cooling steps had a total duration of ∼ 20 min. Afterwards, samples were exposed for 3 min to MWs in an argon atmosphere (step d). During this step the substrates were kept at 200° C by a heater, while the argon pressure was 2 mBar, with a flow of 20 sccm. MWs were generated by a 2.45 GHz Alter Ti Series microwave source, with a power of 450 W. The MW field was guided in a rectangular guide, converted into a TM_{01} mode through a TE/TM converter, and then sent into the CVD reactor. Those conditions sustained the argon plasma. The sample volume was very small (about 0.05 cm^3) compared to the reactor chamber (1500 cm^3) filled with plasma during the process. The standing wave condition was fundamentally determined by the chamber length and by the position of the graphite susceptor, which actually closed the

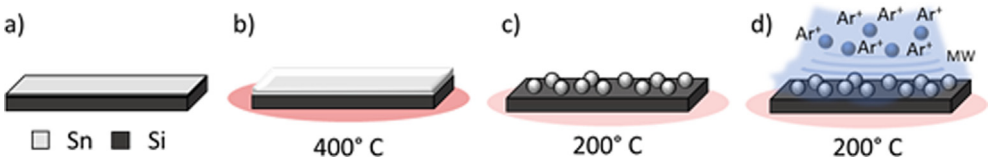

Fig. 1. Sketch of the MW synthetic process steps: a) deposition of an Sn film by thermal evaporation, b) baking: metal melting, c) cooling: Sn nanospheres formation, d) exposure to microwaves in argon atmosphere. Substrate temperature is reported.

transmission line. A boron nitride spacer (between the sample and the susceptor) was used in order to increase the electric field reaching the sample. In these conditions, the sample is not expected to alter appreciably the chamber environment.

It should be remarked that silicon intrinsically absorbs microwaves way less than nanostructured Sn. Moreover, the MWs power was intentionally kept at a low level (500 W). Therefore, bulk silicon was not expected to increase appreciably its temperature. The extremely fast turn on and turn off transients seemed to indicate that heat transfer was limited to the surface. MWs induced a current in the nanospheres, heating the metal through extremely steep rise and fall steps (1900° C/s), while the bulk silicon remained at 200 °C (measured by a METIS M318 Sensortherm infrared pyrometer) [22].

The temperature profile reported in Fig. 2 refers to the silicon area covered Sn film, whereas the bare silicon remains at a lower temperature. The pyrometer measured a maximum surface temperature of 380 °C during baking, whilst it decreased down to 200 °C afterward. When microwaves were switched on, the surface temperature increased abruptly until it stabilized at 270 °C for about four minutes, after which it decreased abruptly again. The samples were kept at 200 °C for more than 20 min (not shown in the figure).

2.2. Transmission electron microscopy

Transmission electron microscopy (TEM) observations were carried out with a Philips CM200 electron microscope equipped with a LaB_6 filament and operating at 200 kV. Samples for TEM observations were prepared in cross-section by the conventional thinning procedure relying on mechanical polishing by grinding papers, diamond pastes, and a dimple grinder. Final thinning was carried out by an ion beam system (Gatan PIPS) using Ar ions at 5 kV. It is important to stress that to perform the mechanical thinning/polishing samples were glued with a special wax at 80–90 °C and that even the final thinning by the ion beam might have given rise to a local heating which is difficult to quantify.

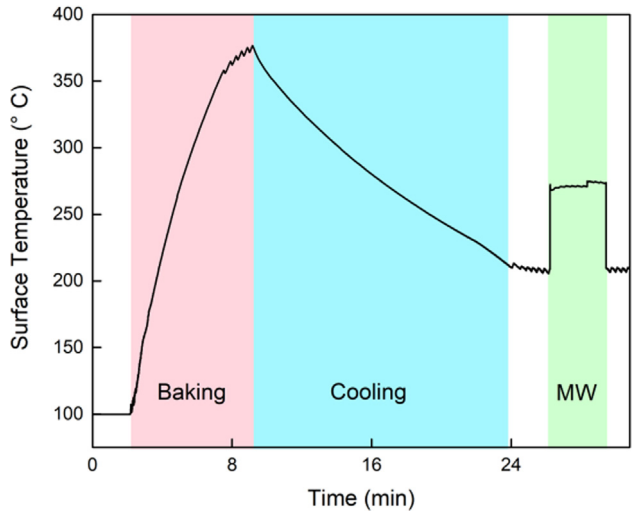

Fig. 2. Temperature profile of the substrate surface during the whole process in the MW-CVD chamber.

2.3. Far-infrared spectroscopy

Far-infrared spectroscopy was performed using a Fourier transform infrared spectrometer (FTIR, Bruker Vertex V80) in vacuum to prevent spectral artifacts due to atmospheric absorption lines [23]. All the samples were mounted on a vacuum-tight translation stage which allows them to be moved sequentially in the focal position of the infrared spectrometer. A relative tilt angle of 15° with respect to the beam propagation direction was monitored with a pilot laser. Misalignment between the two samples was smaller than 1°. The beam spot diameter on the samples was defined by an optical iris and was kept equal to 4 mm in all the measurements. Absorption spectra were collected at room temperature, using a broadband source. The energy range 8–70 meV was characterized using a mylar multilayer beamsplitter and a DTGS (deuterated triglycine sulphate) detector. The 60–600 meV energy range was characterized using a KBr beamsplitter and a DLaTGS (L-alanine DTGS) detector.

2.4. X-ray photoelectron spectroscopy

X-ray Photoelectron Spectroscopy (XPS) was performed by using a Perkin-Elmer Φ 5600ci spectrometer with non-monochromatic Al Kα source (1486.6 eV) to investigate the chemical composition of the silicon samples covered by Sn nanospheres.

2.5. Scanning electron microscopy (SEM) and atomic force microscopy (AFM)

SEM images were acquired with a Zeiss micrograph (model Merlin), equipped with a GEMINI column, using an acceleration voltage of 5 kV and a nominal current of 40 pA.

AFM analysis was performed by means of a Bruker Dimension ICON Nanoscope in Tapping operation mode with a SCM-PIT-V2 silicon cantilever (nominal spring constant 3 N/m, nominal tip radius 25 nm), scan size of the acquired image was 1 μm^2 and scan rate 1.4 Hz.

2.6. X-ray diffraction

XRD data were collected using the Bragg-Brentano geometry [24] by nickel-filtered Philips X'Pert PW 3020 goniometer, equipped with Cu Kα radiation, a graphite monochromator, and a proportional counter with a pulse-height discriminator were used. A 2 rps in-plane sample rotation was used during data collection.

2.7. Secondary ion Mass spectrometry (SIMS)

SIMS depth profiling was performed in order to inspect the presence of Sn atoms in the silicon bulk after MW irradiation. SIMS measurements were done with a CAMECA IMS-4f instrument using

two different experimental setups. In a first trial, a 5.5 keV O_2^+ primary ion beam was employed, detecting positive secondary ions. In a second set of measurements, a 14.5 keV Cs^+ beam was used, detecting negative secondary ions. In both cases, the beam was scanned over a 250 μm^2 square area, detecting secondary ions coming from a 60 μm diameter circular area at the center of the crater to avoid edge artifacts. The time-to-depth conversion was obtained by measuring the crater depth after each measurement with a Tencor P17 mechanical stilus profilometer. A reference ^{28}Si signal from the silicon matrix was acquired during each measurement. Relative Sensitivity Factor from literature [25] was used to obtain a quantitative conversion of the ^{120}Sn- isotope secondary ion yield into concentration vs. depth profiles of the Sn distribution in the silicon bulk. The measurements performed with the O_2^+ beam showed a good depth resolution, but suffered from a lower sensitivity and a higher detection limit. For these reasons, a Cs^+ beam was to investigate the Sn profile.

3. Results

AFM and SEM observations performed at the end of the process showed an almost homogeneous distribution of nanospheres with an average diameter of about 25 nm (Fig. 3a, b). The particle-size analysis performed on SEM images (Fig. 3c) indicated that the nanosphere radii are distributed in the 5–30 nm range. Particle size mean and standard deviation were found to be 11.8 nm and 5.4 nm, respectively. The spacing between adjacent nanoparticles is ~ 10 nm. From the analysis of AFM images (Fig. 3b) a radial distribution from 5 nm to 43 nm, with mean value 13.5 nm and standard deviation 10.1 nm was retrieved. The analysis showed that nanospheres appear to be slightly larger in the AFM image. This can be ascribed to the different lateral resolution of the two imaging systems, which was ~ 4 nm and ~ 10 nm for the employed SEM and AFM systems, respectively.

The nanoparticles displayed in the TEM picture (Fig. 3d, and Fig. 3e) exhibit a core–shell structure, with a thick amorphous oxide layer wrapping the tin sphere core. The tin core diameter lay in the 9–18 nm range, while the whole nanosphere diameter (core + shell) ranges from 23 to 36 nm. These dimensions are in agreement with the average diameter of the nanosphere (25 nm) obtained by AFM and SEM analysis. The oxide shell was probably generated through multiple steps. Indeed, a native oxide seed had already formed when the Sn film was introduced into the CVD chamber. After sphere formation, diffusion of O^{2-} from the underlying SiOx film, favored by MW irradiation, and the high reactivity of Sn nanoparticles, resulted into a further growth of the oxide shell. TEM analysis performed on the nanospheres revealed a flattened form, rather than a perfect spherical shape, with the bottom part of the core in contact with the substrate. The nature and crystallinity of the material inside the NS core were investigated by selected area electron diffraction (SAED) measurements. In particular, Fig. 3f shows the SAED pattern of the NS displayed in Fig. 3c. The most intense diffraction spots belong to the Si substrate in the [1 1 0] zone axis orientation, but few feeble diffraction spots are also visible. TEM dark field images obtained with these extra spots allowed the crystallinity of NS core to be identified. The lattice parameters corresponding to the feeble diffraction spots can be associated to the presence of Sn in the β phase.

As for the infrared optical characterization, four samples were prepared: (i) a pristine intrinsic silicon substrate serving as reference; (ii) the test sample (MW_Sn) with Sn nanospheres irradiated with MWs, (iii) a control sample (MW_SnRemoved) where the nanospheres were exposed to MWs and then removed by HCl and (iv) a control sample (NoMW_Sn) where the Sn nanospheres were not irradiated with MWs. All the silicon substrates employed had the same thickness (350 μm).

In order to estimate the absorbance contribution of the MW irradiated nanospheres, the optical transmittance spectra of the test sample (MW_Sn) were compared with the control ones. The

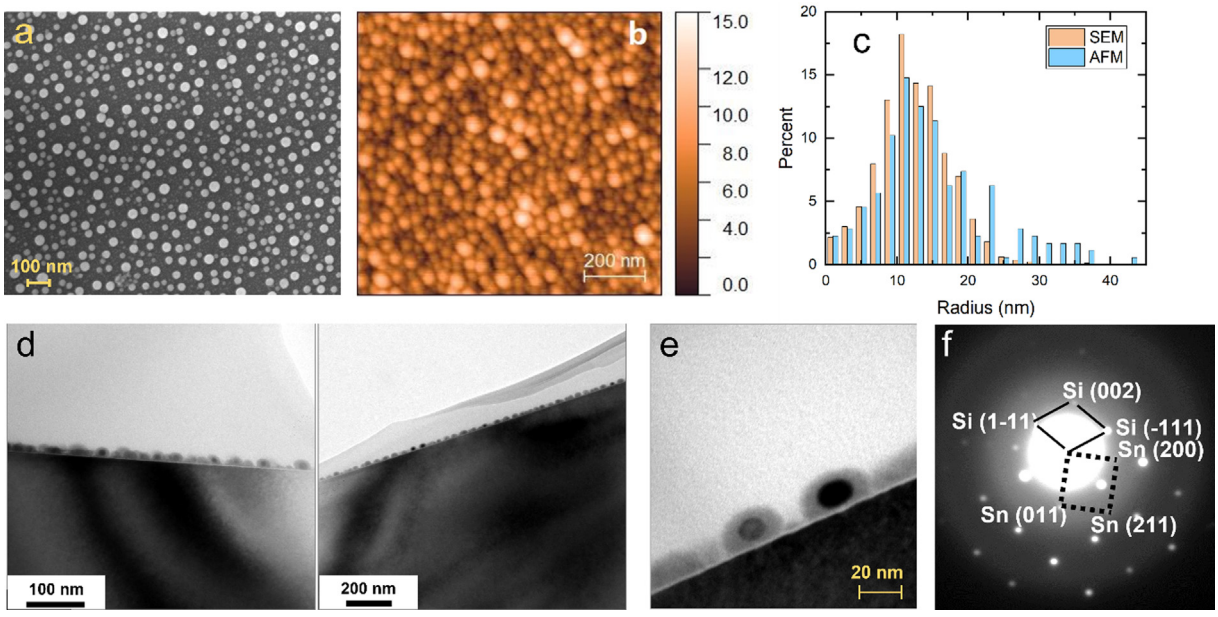

Fig. 3. Sn nanospheres after MW exposure looked over by: a) SEM and b) AFM. c) Distribution of nanosphere radius obtained by particle size analysis performed on SEM and AFM images. The analysis was conducted on an ensemble of 880 and 260 nanospheres in the SEM and in the AFM cases, respectively. d)TEM bright field cross-sectional images of Sn nanospheres, at different magnifications, on silicon substrate after micro-waves exposure. The core–shell structure of the nano-spheres is clearly visible. The tin core has a darker contrast than the surrounding amorphous shell. The higher or lower contrast of the core in the different nanospheres depends on the different crystallographic orientation of the tin core (diffraction contrast) and on the way the nanosphere is cut during the sample preparation. e) TEM image and f) SAED pattern focusing on a few nanospheres: Si [1 1 0] continuous cell; Sn [0–11] dotted cell.

variation of absorbance with respect to the unprocessed silicon substrate (reference) was estimated for each measured sample (test or control) as $\alpha = 1 - T_{sample} / T_{ref}$, where T_{sample} and T_{ref} are the transmittance spectra.

The result of FTIR measurements on the MW_Sn test sample is shown in Fig. 4a, while in Fig. 4b and Fig. 4c results from control samples NoMW_Sn and MW_SnRemoved are reported for comparison. The absorbance is plotted as a function of photon energy (and frequency) in the 20–640 meV energy range. The plot corresponding to the test sample irradiated with MW (Fig. 4a) showed an absorption edge between 40 and 80 meV (10–20 THz), with α greater than 10% for a photon energy larger than 70 meV. On the contrary, the control samples NoMW_Sn (Fig. 4b) and MW_SnRemoved (Fig. 4c) exhibited a small variation of absorbance with respect to the reference sample (α less than 4%) across the investigated frequency range. The absorption edge in Fig. 4a was attributed to the narrow bandgap of the MW-irradiated tin nanospheres.

In order to further prove this statement, the well-established Tauc formalism [26,27] was exploited to estimate the band gap energy of the irradiated material inside the nanospheres, starting from data in Fig. 4a (set MW_Sn). The Tauc equation [26] was used: $(\alpha \cdot h\nu)^{1/\gamma} = B(h\nu - E_g)$, where h is the Planck constant, ν is the photon frequency, $h\nu$ is the photon energy, E_g is the band gap energy, B is a fitting parameter, and γ depends on the nature of the optical transition. In particular, γ is equal to 1/2 and 2 for direct and indirect transitions, respectively. In Fig. 4d, direct (dashed line) and indirect (dotted line) bandgap fitting are compared to the experimental data from MW_Sn sample (red circles). Data fitting outlines that $\gamma = 1/2$ (dashed line) approximates the obtained optical spectra better than $\gamma = 2$ (dotted line). This indicates that the material bandgap is direct. Furthermore, Tauc equation fitting allows for the extraction of the energy gap value, which is $E_g = 52 \pm 1$ meV.

In conclusion, from the infrared spectroscopy analysis, a narrow (52 meV) bandgap could be measured for the sample with Sn nanospheres exposed to microwaves. Moreover, it can be reasonably stated from data fitting that the investigated material possesses a direct bandgap.

Furthermore, the MW treatment results into Sn nanospheres stable at temperatures up to 200 °C and with a non-zero direct bandgap. Such structure and properties can be reasonably ascribed to the formation of tin α-phase. It is worth noticing that this phase is generally stable only below 13°. However, it has been reported that α-Sn can be stabilized at higher temperature by means of epitaxial growth on proper substrates or strain stemming from host contamination. Furthermore, the particle size can also affect the bandgap. On the other hand, interaction between silicon and tin are hindered by Si and Sn extremely low reciprocal solubility.

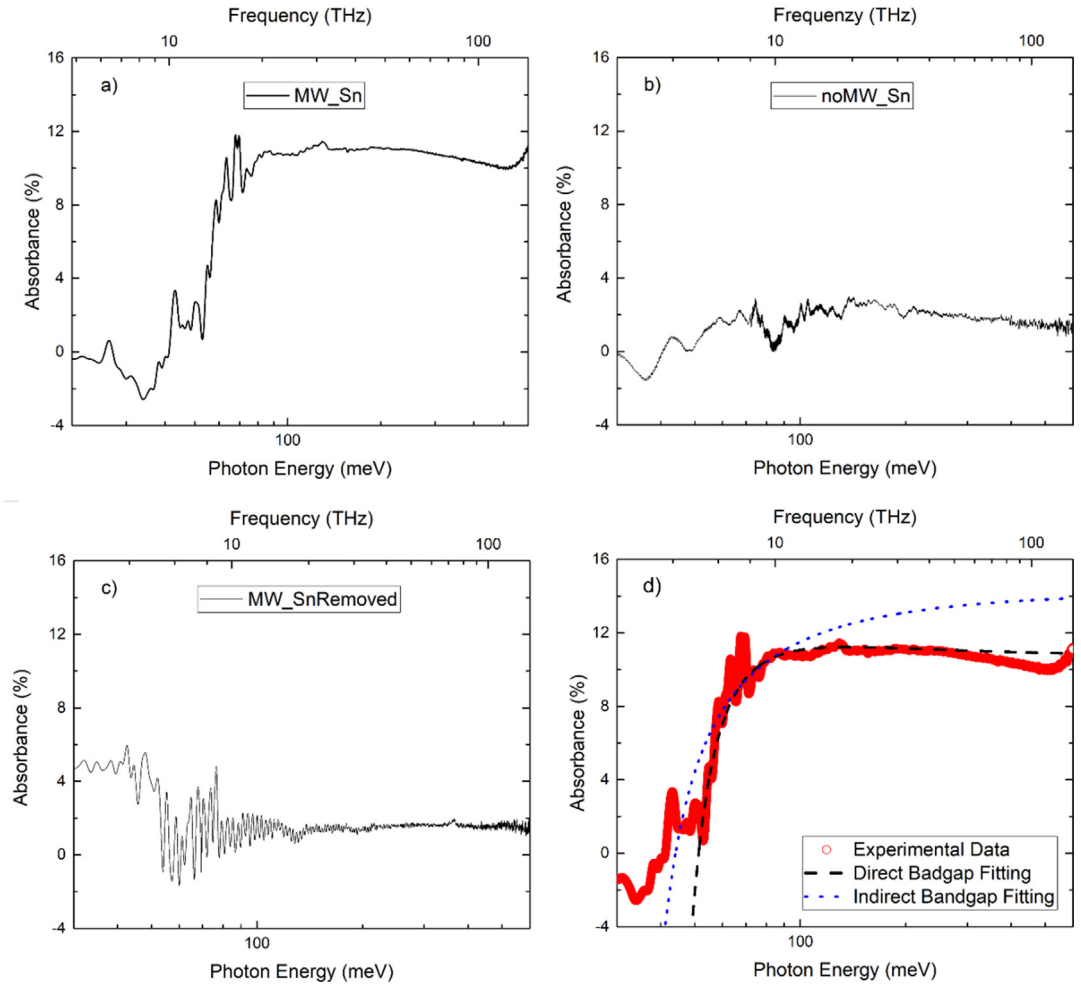

Fig. 4. Optical absorption spectra of: a) test sample with Sn NSs irradiated with MW (MW_Sn); b) control sample with Sn NSs not irradiated with MW (NoMW_Sn); c) control sample irradiated with MW (set a)) after Sn NSs removal (MW_SnRemoved). d) Tauc equation data fitting of optical absorption spectrum from sample with Sn NSs irradiated with MW (MW_Sn). Red circles indicate experimental data, dashed and dotted lines refer to the direct bandgap fitting and indirect bandgap fitting, respectively. (For interpretation of the references to colour in this figure legend, the reader is referred to the web version of this article.)

Indeed, solubility of Si in Sn is less than 10^{-5} at. % at eutectic temperature and solubility of Sn in Si is 0.1 at. % at 1000 °C. Nonetheless, it has been widely reported that microwave assistance allows for faster and more cost-effective synthesis solutions than standard methods and may cause different effects [28,29]. Microwave heating can occur in solid state electronic and ionic conductive materials, through atomic diffusion enhancement [30,31] and multiphonon interactions [32]. Therefore, MWs are supposed to facilitate Si and Sn interdiffusion. Results displayed in Fig. 4 demonstrated that before MW irradiation the Sn nanospheres did not show optical properties related to the presence of the α-phase. In addition, it should be noticed that the large atomic radius difference between Si and Sn (110 and 130 ppm, respectively) may be responsible for a strain in the unit cells of both materials [33].

Before and after MWs exposure, XPS quantitative analysis revealed the presence of Sn, Si, O, and C. In both samples the XPS quantitative analysis led to the same results, provided that experimental errors are taken into account: 18% Sn, 5% Si, 47% O, and 30% C. Carbon is mainly due to adventitious contamination, commonly present on all samples exposed to environmental air and originating a C1s signal centered around 284.8 eV of binding energy, BE (Fig. I in Supporting Information). This marked signal is the consequence of the very high surface sensitivity of the XPS technique (sampling depth ~ 5 nm). Silicon is detected in two different chemical states, namely SiO_x and Si, related to Si2p components centered at 102.1 eV and 99.0 eV of BE, respectively (Fig. I in Supporting Information). As reported above, the detected amount of tin is roughly 3–4 time larger than silicon, confirming an almost complete coverage of the Si wafer surface by Sn.. As for Sn chemical state, the XPS analysis revealed no changes before and after MWs exposure (Fig. 5): in both samples the $Sn3d_{5/2}$, related to tin bonded to oxygen, was detected at BE = 486.9 eV. Although the high BE value detected is usually attributed to Sn^{4+}, the $Sn3d_{5/2}$ binding energy difference between SnO and SnO_2 is not large enough for the two compounds to be distinguished. Moreover, the detected amount of oxygen as well as its binding energy are consistent with the presence of SnO_2 (Fig. I in Supporting Information). Considering the limited sampling depth of XPS and being the thickness of the amorphous shell around nanoparticles thicker than 7 nm (see Fig. 3e), it can be safely stated that the detected tin signal belongs to the external amorphous region of the nanospheres. Thus, the outer shell of the tin nanosphere seems to be made out of SnO_2. For the same reason, the nanoparticle core composition could not be determined.

Comparing these evidences with the experimental findings obtained through the other investigation techniques, the MWs appear to affect mostly the nanosphere core, especially because of the large difference between the melting temperatures of Sn and SnO_2 (231.9° C and 1127° C for bulk Sn and SnO_2, respectively).

Sn depth profile from sample surface to bulk Si was successfully investigated by Secondary Ion Mass Spectroscopy (SIMS). Three curves obtained under identical experimental conditions from three different samples are reported in Fig. 6. The curve with blue symbols refers to a sample with Sn NSs after MW irradiation (MW_Sn). A high Sn concentration peak, connected to the Sn NSs, was detected in the first ~ 10 nm underneath the surface, whilst a long exponentially decreasing tail was found to extend inside the silicon bulk. This tail was mainly due to the ion beam mixing induced by the high energy Cs^+ ions, which redistributed the Sn atoms from the surface to a maximum depth of about 120 nm. A similar tail was also observed when O_2^+ Primary ions were used. Nonetheless, the Sn distribution extended to a maximum depth of about 50 nm. Thus, the depth resolution for O_2^+ was at least twice better than the one achieved by the Cs^+ beam because of the much lower energy of the primary beam. The curve with black dots refers to a similar sample, which had been treated with an HCl solution after MW irradiation, in order to remove the Sn NSs from the surface while keeping intact the underlying silicon substrate (MW_SnRemoved). The measured Sn profile showed again a residual concentration of Sn on the surface, followed by a peak immediately beneath and a tail extending to about 60 nm in depth. Tin concentration associated to the Sn peak below the surface was ~ $1x10^{18}$ cm^{-3}. The curve with orange symbols refers to bare Si irradiated with MWs (MW_BareSi), which served as a control sample to estimate the possible presence of surface contaminants. In fact, also this sample showed the presence of Sn on the surface and an in-depth tail with a maximum concentration beneath the surface of about $1x10^{17}$ cm^{-3}. This (almost negligible) Sn signal in a pristine sample might be related either to surface contamination during sample preparation (and/or manipulation) or to measuring chamber contamination. Subtracting the contribution of surface contaminants from the other two curves, the Sn profile after HCl etching (black symbols) clearly showed that an Sn

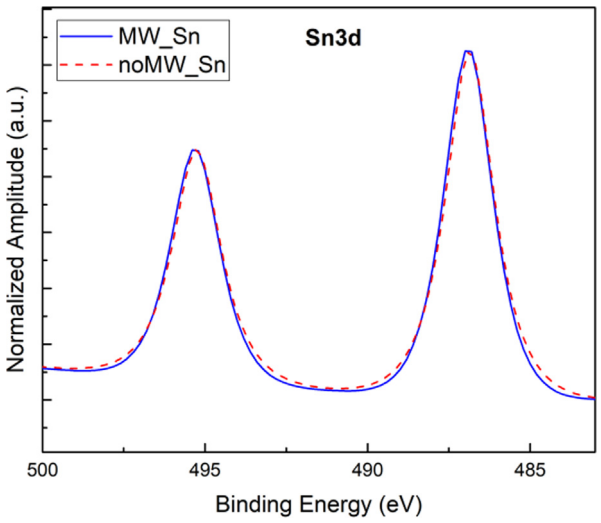

Fig. 5. XPS spectra of Sn3d in the sample after (MW_Sn, blue solid line) and before (noMW_Sn, red dashed line) the MW exposure. (For interpretation of the references to colour in this figure legend, the reader is referred to the web version of this article.)

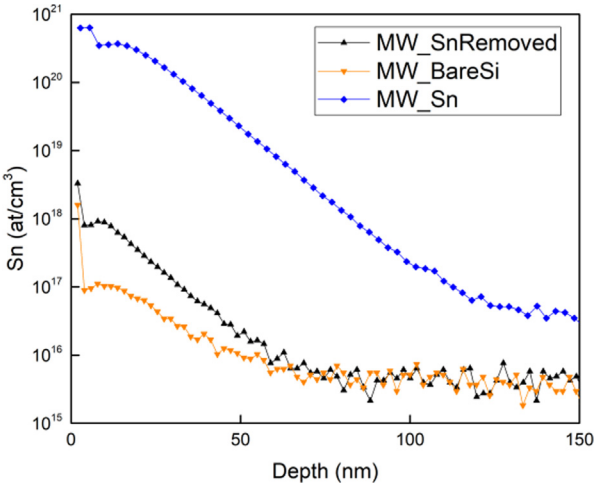

Fig. 6. Sn depth profiles for three different samples after MW irradiation: with Sn nanospheres (MW_Sn); after Sn nanospheres removal (MW_SnRemoved); Si reference sample, without deposition of Sn (MW_BareSi).

amount in the order of 10^{18} cm^{-3} was still present in the near-surface region. Sn penetration depth into the Si substrate was found to be in the order of few tens of nanometers. These results were attained by taking into account the depth resolution of the SIMS in this measurement compared to the one obtained with the O_2^+ beam (which also showed an Sn accumulation underneath the surface).

XRD results, shown in Fig. 7, highlighted the effect of Sn nanospheres presence. Fig. 7a compares two different portions of the same sample (10^{16} cm^{-3}p-doped silicon substrate), differing only for the presence of Sn nanospheres. The bare portion exposed to MWs (MW_BareSi) is represented with an orange line, whereas the part with the Sn nanospheres on top and exposed to MWs (MW_Sn) is represented with a purple line. In addition, an Al sheet shield was used (peaks marked with rhombi in Fig. 7a belongs to the Al shield) in order to tell apart the contributions of the two different parts. The peak of the silicon diamond phase (at 2θ = 69.2°) is dominant. Nevertheless, in the MW_Sn portion, a side peak at 2θ ≈ 33°, which could not be ascribed to any other material involved, was detected. An additional sample completely covered by Sn nanospheres and treated with MWs was analyzed to attain a higher quality spectrum. Fig. 7b-c provide a detailed diffraction pattern of this sample in the 20–60 and 114-120° 2θ ranges respectively. Specifically, peaks at 2θ ≈ 33° and 2θ ≈117° are present. Noticeably, the same results were found with both n-doped and intrinsic silicon. Those two peaks were narrow enough to distinguish the two components of the Cu Kα radiation ($K\alpha_1$ and $K\alpha_2$), implying a high degree of crystallinity of the material. In literature, the peak at 2θ = 32.98° is commonly attributed to silicon 200 forbidden reflections stemming from instrumental artifacts [34] or to lattice distortion [35]. However, instrumental effects can be safely ruled out because the peak 2θ = 32.98° does not appear in the MW_Bare Si diffraction pattern. Therefore, presence of Sn nanospheres can reasonably account for silicon lattice distortion and, consequently, for the XRD peak. Nonetheless, diffraction peaks belonging to Sn-bearing phases are not visible, probably due to the extremely small volume of the Sn nanoparticles. A second set of experiments was performed on silicon samples coated with a 70 nm-thick SiOx layer. Sample were analyzed after every step of the synthetic procedure. Thus, Fig. 7d reports a bare sample before the Sn deposition (Substrate, black curve); a sample with Sn nanospheres on top before MW treatment (NoMW_Sn, red curve) and the same sample after the MW treatment (MW_Sn, blue curve). The peak at about 33° was detected only in MW treated sample. The absence of the 2θ = 32.98° peak once again excludes instrumental effects. The two additional peaks at 2θ = 34.3° and 2θ = 37.1° can be attributed to the bare substrate (black curve in Fig. 7d). In conclusion, the two sets of experiments prove that the distortion takes place only when both Sn deposition and MW treatment are performed. Furthermore, it can be also affirmed that the distorted material has an extended volume, since the amplitude of the 33° peak is a significant fraction of the main Si-I peak.

4. Discussion

MW exposed silicon substrates with Sn nanospheres uniformly distributed on the surface revealed an optical absorption edge between 40 and 80 meV. Furthermore, data fitting indicates a direct energy bandgap of about 52 meV. α-Sn domains were likely formed inside the nanospheres. Indeed, although the SAED measurements revealed only the presence of the metallic phase, it should be emphasized that during the preparation for TEM analysis, the samples were submitted to thermal treatments (as described in the Materials and Characterization section). Moreover, the low thickness of the sample (needed for the material to be electron transparent) tends to relax any possible internal stress. The combination of all these factors is sufficient to promote a transition from the metastable α-Sn to the stable β-Sn. The bandgap of α-Sn and its (meta) stability range can be affected by multiple factors, such as the size of the nanoparticle that can induce quantum confinement [11] and the specific strain derived from the insertion of host atoms. [9,18,19]. Since a smaller bandgap compared to literature was obtained, a low quantum confinement effect can be inferred, thus implying an α-Sn domains extension comparable to Bohr exciton radius (12.56 nm [11]). Neither bare silicon exposed to microwaves, nor pristine Sn nanospheres on Si revealed the presence of such an "exotic" phase. Therefore, at this stage of the research, a phenomenological picture based on the experimental evidence collected during several tests can be provided. MWs can induce a selective heating of the metallic material, bringing about melting of the Sn nanoparticle inner part, while keeping the silicon substrate at lower temperatures. The interaction with microwaves and the abrupt increase of surface temperature (Fig. 2), can facilitate the diffusion of Si atoms from the surface towards the nanosphere cores [30,31]. It can be deduced that the innermost core of the droplets, in direct contact with the silicon substrate, is subjected to a relatively high temperature promoting silicon and tin interdiffusion. A similar increase in temperature has already been reported in Refs. [8,36]. Furthermore, stabilization of

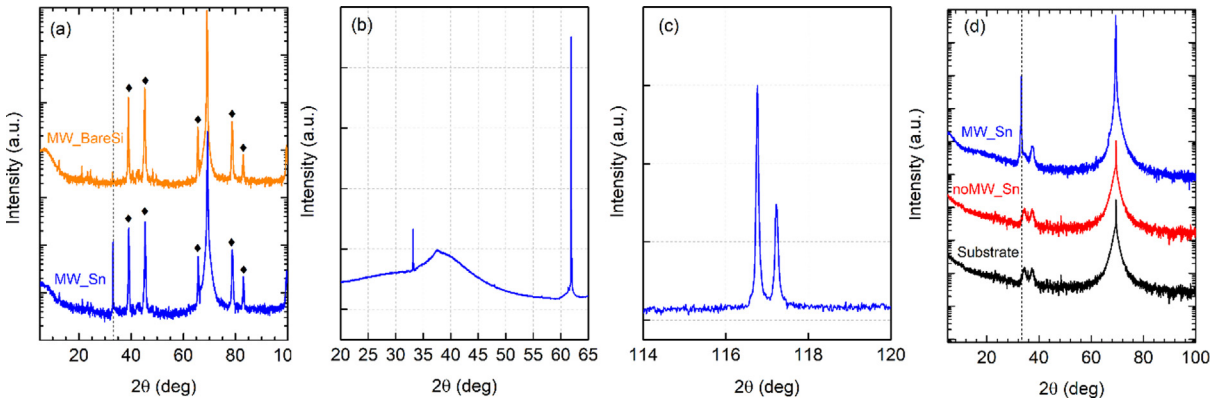

Fig. 7. (a) XRD spectra of samples MW_Sn (blue line) and MW_bareSi (orange line); peaks marked with rhombi belong to the Al shield; the 2θ = 33° peak is marked by a dashed line. (b-c) Zoom of the peaks of an additional sample completely covered by Sn nanospheres and treated with MWs around (b) 2θ = 33° and (c) 2θ = 117°; (d) spectra at different steps of the process for an SiO_x covered sample: the bare substrate without Sn on top (Substrate, black line), the same substrate with Sn nanospheres on top before (NoMW-Sn, red line) and after MW exposure (MW_Sn, blue line). (For interpretation of the references to colour in this figure legend, the reader is referred to the web version of this article.)

the α-phase by Si trapping in Sn due to MW induced quenching can be hypothesized, it has already been reported by other authors [12,20,37–38]. The extremely steep heating and cooling edges (1900 °C/s) on the Sn nanospheres may favor the diffusion of Sn atoms into the silicon crystalline lattice (as seen by SIMS), and simultaneously hinder atomic re-arrangement. Consequently, the rapid cooling during the fabrication process may "freeze" the structure in a metastable condition. Once MWs are switched off, fast quenching takes place, possibly leading to an instantaneous stabilization of the α-phase [11].

It should be noted the material in the nanospheres is not pure, being comprised of a Sn core possibly doped with silicon and an amorphous oxide shell, which may perhaps bring some benefit in practical applications, by passivating the active material.

In addition, it can be noticed that tin atoms included into the Si cells cause a compressive strain in the host material (because of the different atomic radius and atomic number [33]), which accounts for the two peaks in the XRD pattern. The 33° and 117° XRD peaks (Fig. 7), can be justified by a wide silicon lattice distortion ascribed to the inclusion of Sn atoms. Hence, MW-driven Si inclusion in Sn, and the consequent induced strain, could be responsible for the formation a α-tin phase stable up to 200 °C [39] with a direct bandgap of 52 meV. The energy gap obtained with the current size of nanoparticles lies in a range corresponding to a free space wavelength between 20 and 35 μm, *i.e.* in the far-infrared region between the mid-infrared (MiR: ≈ 2–20 μm) and terahertz (THz: ≈ 60 – 300 μm). This energy range is suitable for spectroscopic sensing applications such as radiation detection in astrophysics and environmental monitoring [40]. However, the technological development in this range of wavelengths is hampered by the highly dispersive and absorptive optical response of III-V semiconducting crystals. In fact, the strong interaction of incident photons with lattice vibrations, which gives rise to a frequency gap known as the Reststrahlen band, occurs at these wavelengths [41].

Finally, the possibility of tuning the direct band gap and the absorption cutoff by controlling the particle size, the Si atoms inclusion and the interaction with microwaves, would be of paramount importance. Indeed, such features can be exploited for the fabrication of optoelectronic devices in the IR spectrum towards integrated applications for a monolithic platform on silicon.

5. Conclusions

Irradiation by microwaves of a random distribution of Sn nanospheres on silicon was the basis for the formation of an exotic tin α-phase with narrow bandgap of about 50 meV. This phase appears to have a direct bandgap and turned out to be stable at least up to 200 °C. Experiments demonstrated that microwaves are instrumental in synthesizing the α-phase synthesis. Indeed, metastable phase stabilization brought about by abrupt temperature rises and drops, possibly in conjunction with Si inclusion in Sn nanospheres, seems to be likely explanation. Further studies are required to get a deeper insight of the mechanism leading to the α-Sn formation. For instance, thicker Sn depositions (provided that Sn nanospheres are still formed), together with more sophisticated analyses, such as Mossbauer Spectroscopy and Atom Probe Tomography, could clarify the impact of the different synthetic parameters on final exotic phase. Band gap tuning relying on different particle size can also be attempted. Moreover, metal layer patterning can pave the way to potential integration in optoelectronic manufacturing. The ability of precisely and simultaneously controlling the particle geometry and electronic bands in these α-Sn systems would allow a large variety of low-dimensional systems to be developed. Such nanostructures are versatile building blocks for silicon compatible infrared detectors, sensors, and emitters, with applications in free-space communication, infrared energy harvesting, biological and chemical sensing, and thermal imaging. Being the proposed MW driven synthesis a large-scale, low-temperature process, compliant with the complementary metal-oxide semiconductor (CMOS) technology, it can play a significant role in implementing a new generation of cost-effective mid/far-IR platforms.

Data availability

The raw/processed data required to reproduce these findings cannot be shared at this time as the data also forms part of an ongoing study.

Declaration of Competing Interest

The authors declare that they have no known competing financial interests or personal relationships that could have appeared to influence the work reported in this paper.

References

[1] D. Benedikovic, L. Virot, G. Aubin, J.-M. Hartmann, F. Amar, X. Le Roux, C. Alonso-Ramos, É. Cassan, D. Marris-Morini, J.-M. Fédéli, F. Boeuf, B. Szelag, L. Vivien, Silicon–germanium receivers for short-wave-infrared optoelectronics and communications, Nanophotonics 10 (3) (2021) 1059–1079.
[2] E. Kasper, Prospects and challenges of silicon/germanium on-chip optoelectronics, Front. Optoelectron. in China 3 (2) (2010) 143–152.
[3] J. Liu, R. Camacho-Aguilera, J.T. Bessette, X. Sun, X. Wang, Y. Cai, L.C. Kimerling, J. Michel, Ge-on-Si optoelectronics, Thin Solid Films 520 (8) (2012) 3354–3360.
[4] P. Velha et al., Strained germanium nanostructures on silicon emitting at >2.2 μm wavelength, 10th International Conference on Group IV Photonics (2013) 142–143.
[5] O. Moutanabbir et al., Monolithic infrared silicon photonics: the rise of (Si) GeSn semiconductors, Appl. Phys. Lett. 118 (11) (2021) 110502.
[6] S. Barth et al., Microwave-assisted solution–liquid–solid growth of Ge 1–x Sn x nanowires with high tin content, Chem. Commun. 51 (61) (2015) 12282–12285.
[7] S. Kasap, P. Capper, Handbook of electronic and photonic materials, Springer, 2017.
[8] E. Kasper et al., Germanium tin: silicon photonics toward the mid-infrared, Photonics Res. 1 (2) (2013) 69–76.
[9] Carrasco et al., The direct bandgap of gray αtin investigated by infrared ellipsometry, Appl. Phys. Lett. 113 (23) (2018) 232104.
[10] F. Oliveira, Photonic integrated circuit (PIC) devices for inter- and intra-chip optical communication using GeSn alloy layers grown on Silicon substrates (2011).
[11] A.U. Haq et al., Size-dependent stability of ultra-small α-/β-phase tin nanocrystals synthesized by microplasma, Nat. commun. 10 (1) (2019) 1–8.
[12] W.M.T. Gallerneault, F. Vnuk, R.W. Smith, Silicon-stabilized grey tin, J. appl. phys. 54 (7) (1983) 4200–4201.
[13] A. Barfuss et al., Elemental topological insulator with tunable Fermi level: Strained α-Sn on InSb (001), Phys. rev. lett. 111 (15) (2013) 157205.
[14] N. Oehl, L. Hardenberg, M. Knipper, J. Kolny-Olesiak, J. Parisi, T. Plaggenborg, Critical size for the β-to α-transformation in tin nanoparticles after lithium insertion and extraction, Cryst. Eng. Comm. 17 (19) (2015) 3695–3700.
[15] X.u. Cai-Zhi et al., Elemental Topological Dirac Semimetal: α-Sn on InSb(111), Phys. rev. lett. 118 (14) (2017) 146402.
[16] D.T. Wang, N. Esser, M. Cardona, J. Zegenhagen, Epitaxy of Sn on Si (111), Surf. sci. 343 (1-2) (1995) 31–36.
[17] B.R. Cuenya et al., Epitaxial growth and interfacial structure of Sn on Si (111)-(7x 7), Surf. sci. 506 (1-2) (2002) 33–46.
[18] H. Huang, F. Liu, Tensile strained gray tin: Dirac semimetal for observing negative magnetoresistance with Shubnikov–de Haas oscillations, Phys. Rev. B 95 (20) (2017) 201101.
[19] I. Madaveric et al., Structural and electronic properties of the pure and stable elemental 3D topological Dirac semimetal α-Sn, Apl Mater. 8 (3) (2020) 031114.
[20] M. Bürkle et al., Tuning the Bandgap Character of Quantum-Confined Si–Sn Alloyed Nanocrystals, Adv. Funct. Mater. 30 (22) (2020) 1907210.
[21] B.R. Cuenya et al., Structure and vibrational dynamics of interfacial Sn layers in Sn/Si multilayers, Phys. Rev. B 64 (23) (2001) 235321.
[22] Palma, F. US Patent App. 16/648,080, 2020.
[23] D.M. Slocum, E.J. Slingerland, R.H. Giles, T.M. Goyette, Atmospheric absorption of terahertz radiation and water vapor continuum effects, J. Quant. Spectrosc. Ra. 127 (2013) 49–63.
[24] D.L. Bish, J.E. Post, Modern powder diffraction, Walter de Gruyter GmbH & Co KG, 2018.
[25] F. Stevie, Secondary ion mass spectrometry: applications for depth profiling and surface characterization, Momentum Press, 2015.

[26] P. Makuła, M. Pacia, W. Macyk, How To Correctly Determine the Band Gap Energy of Modified Semiconductor Photocatalysts Based on UV−Vis Spectra, J. Phys. Chem. Lett. 9 (23) (2018) 6814–6817.
[27] T. Wang, B. Daiber, J.M. Frost, S.A. Mann, E.C. Garnett, A. Walsh, B. Ehrler, Indirect to direct bandgap transition in methylammonium lead halide perovskite, Energy Environ. Sci. 10 (2) (2017) 509–515.
[28] A. Kumar, Y. Kuang, Z. Liang, X. Sun, Microwave chemistry, recent advancements, and eco-friendly microwave-assisted synthesis of nanoarchitectures and their applications: a review., Materials Today, Nano 11 (2020) 100076, https://doi.org/10.1016/j.mtnano.2020.100076.
[29] H.J. Kitchen et al., Modern microwave methods in solid-state inorganic materials chemistry: from fundamentals to manufacturing, Chem. Rev. 114 (2) (2014) 1170–1206.
[30] S. Vaucher, R. Nicula, J.-M. Català-Civera, B. Schmitt, B. Patterson, In situ synchrotron radiation monitoring of phase transitions during microwave heating of Al-Cu-Fe alloys, J. Mater. Res. 23 (1) (2008) 170–175.
[31] A. Malhotra, M. Hosseini, S. Hooshmand Zaferani, M. Hall, D. Vashaee, Enhancement of diffusion, densification and solid-state reactions in dielectric materials due to interfacial interaction of microwave radiation: theory and experiment, ACS Appl. Mater. Inter. 12 (45) (2020) 50941–50952.
[32] G.R. Robb et al., Temperature-resolved, in-situ powder X-ray diffraction of silver iodide under microwave irradiation, Phys. Chem. Comm. 5 (19) (2002) 135–137.
[33] W. Chen et al., Incorporation and redistribution of impurities into silicon nanowires during metal-particle-assisted growth, Nat. commun. 5.1 (2014) 1–7.
[34] P. Zaumseil, High-resolution characterization of the forbidden Si 200 and Si 222 reflections, J. appl. crystallogr. 48 (2) (2015) 528–532.
[35] L. Zhao, M. Steinhart, M. Yosef, S.K. Lee, T. Geppert, E. Pippel, R. Scholz, U. Gösele, S. Schlecht, Lithium niobate microtubes within ordered macroporous silicon by templated thermolysis of a single source precursor, Chem. Mater. 17 (1) (2005) 3–5.
[36] P. Moontragoon et al., Band structure calculations of Si–Ge–Sn alloys: achieving direct band gap material, Semicond. Sci. Tech. 22 (7) (2007) 742.
[37] M. Lozac'h, V. Švrček, S. Askari, D. Mariotti, N. Ohashi, T. Koganezawa, T. Miyadera, K. Matsubara, Semiconducting silicon-tin alloy nanocrystals with direct bandgap behavior for photovoltaic devices, Mater. today energy 7 (2018) 87–97.
[38] H. A., Atwater, Formation of direct energy gap group IV semiconductor alloys and quantum dot arrays in Sn_xSi_{1-x}/Si and Sn_xGe_{1-x}/Ge alloy systems, MRS OPL, 583.1 (1999) 349-360.
[39] T.D. Eales, I.P. Marko, S. Schulz, E. O'Halloran, S. Ghetmiri, W. Du, Y. Zhou, S.-Q. Yu, J. Margetis, J. Tolle, E.P. O'Reilly, S.J. Sweeney, Ge1− xSnx alloys: consequences of band mixing effects for the evolution of the band gap Γ-character with Sn concentration, Sci. rep. 9 (1) (2019), https://doi.org/10.1038/s41598-019-50349-z.
[40] D. Farrah et al., Review: far-infrared instrumentation and technological development for the next decade, JATIS 5 (2) (2019) 020901.
[41] K. Feng, W. Streyer, Y. Zhong, A.J. Hoffman, D. Wasserman, Photonic materials, structures and devices for Reststrahlen optics, Opt. Express 23 (24) (2015) A1418, https://doi.org/10.1364/OE.23.0A1418.